2016-01-01

Dielectric Prism Antenna

Jose Antonio Avila
University of Texas at El Paso, jaavila5@miners.utep.edu

DIELECTRIC PRISM ANTENNA

JOSE ANTONIO AVILA

Master's Program in Electrical Engineering

APPROVED:

Raymond Rumpf, Ph.D., Chair

Virgilio Gonzalez, Ph.D.

Son-Young Yi, Ph.D.

Charles Ambler, Ph.D.
Dean of the Graduate School

Dedication

This work is dedicated to my family whose love, support and patience has pushed me to accomplish so much.

DIELECTRIC PRISM ANTENNA

by

JOSE ANTONIO AVILA

THESIS

Presented to the Faculty of the Graduate School of

The University of Texas at El Paso

in Partial Fulfillment

of the Requirements

for the Degree of

Master of Science

Department of Electrical and Computer Engineering

THE UNIVERSITY OF TEXAS AT EL PASO

May 2016

Acknowledgements

Thank you, Dr. Rumpf, Carlos Rodriguez, Cesar Valle, Ubaldo Robles, Eric Berry for their help and the rest of the members of the EM Lab as well. I would also like to thank Laird Technologies and NPS. Most of all thank you to my family who made this possible.

Abstract

3D printing is revolutionizing the development and manufacturing of devices. Currently multi-material 3D printing, like metals plus dielectrics, is in the early stages and not very accessible. This work set out to develop an all-dielectric antenna that could be 3D printed with current widely accessible 3D printing technologies. The antenna developed is an all-dielectric ultra-thin antenna with a simple geometry. The antenna radiates by using total internal reflection and a circulating mode operating as a leaky whispering gallery mode. We are calling the antenna the dielectric prism antenna because it acts like an optical prism. The dielectric prism antenna was developed in stages with increasing complexity. First, a one dimensional simulation of a slab waveguide analysis was performed to answer if a usable guided mode was present. Then a two dimensional simulation using finite-difference frequency domain method to visualize steady state fields. The design of the antenna was finalized in a rigorous 3D simulation with the commercial software package, ANSYS HFSS. The antenna was then manufactured and tested resulting in a dielectric prism antenna with a thickness of 1.5 mm operating at 2.4 GHz.

Table of Contents

List of Figures

Chapter 1: Introduction

3D printing is changing manufacturing. The manufacturing process has become more accessible with 3D printers being widely available. This work aimed to design an antenna that could be 3D printed. The antenna designed is an all-dielectric ultra-thin antenna that operates like a prism and is being called the dielectric prism antenna (DPA). Because having an ultra-thin design, 1.5 mm in the design presented, makes it difficult to establish a resonance with traditional designs, a novel design taking advantage of total internal reflection (TIR) is used in order to establish a leaky whispering gallery mode. The DPA presented in this work is of simple geometry and therefore can be easily 3D printed, in this work the printing process of fused deposition modeling (FDM) was utilized. The antenna was designed to operate at a frequency of 2.4 GHz in order to perform a test with WiFi. It was designed to be ultra-thin in order to save on materials and time, also a monolithic all-dielectric design was implemented in order to try to avoid any post-processing in manufacturing or extra tools. The DPA was designed in stages with increasing complexity. The computational methods used in this work utilized the finite-difference approximation to solve Maxwell's equations. First, a one dimensional analysis was performed using slab waveguide analysis. This in order to find if a guided mode existed in a thin slab of dielectric that could be used for TIR. Second, a two dimensional simulation was performed with the finite-difference frequency domain method and the steady state fields where visualized. This step was to confirm if the DPA would resonate. The final design step was a three dimensional rigorous simulation using the commercial package ANSYS HFSS. This work implemented a proof of concept antenna utilizing low-loss dielectric powder from Laird Technologies. A shell was 3D printed through FDM with a Makerbot Replicator 2x. The shell was then packed with dielectric powder and then sealed. Finally, the DPA was tested using a vector network analyzer (VNA), reflectance and pattern measurements were performed. The final test was a WiFi where a stock antenna was replaced with the DPA and a print job was submitted wirelessly. Both the manufacturing and testing took place at the University of Texas at El Paso EM Lab.

1.1 BACKGROUND

1.1.1 3D Printing

3D printing is a developing technology that offers many benefits. It is a widely accessible process that can be performed by anyone. It allows more freedom in complexity of the design allowing for more geometries and a high level of customization that weren't possible before. 3D printing uses inexpensive materials and it allows for rapid prototyping because the manufacturing does not require outsourcing. Currently hybrid 3D printing, simultaneous printing of metals plus dielectric, is in the early stages and is not widely accessible so the cost is very high. Research with 3D printing antennas is being performed at this time using different methods. In [1] an antenna was 3D printed out of Acrylonitrile Butadiene Styrene (ABS) and after a silver painting metallization layer was applied in order to make a radiating element. In [2] an antenna printed with polylactic acid (PLA) and coated with a carbon based conductive black paint is presented. [3] presents a conical spiral antenna 3D printed of PLA and silver nanoparticle ink. [4] presents a bowtie antenna 3D printed with PLA and conductive ABS. In [5] micro-dispensing of conformal antennas is being explored. For the purposes of this work the aim is to keep the 3D printing process as accessible and simple as possible so a simple FDM printer, Makerbot Replicator 2x, is utilized.

1.1.2 Dielectric Antennas

Dielectric antennas are desirable because they have very low loss and thus are efficient radiators. The dielectric material is also inexpensive and widely available. There are various forms of dielectric antennas, in [6] an all-dielectric horn antenna of electromagnetic bandgap structure with evanescent feeding is presented. In [7] a dielectric rod antenna is designed for ultra-wideband operation and [8] presents a leaky-wave dielectric antenna. In [9] the most compact of the dielectric antennas is presented with the dielectric resonator antenna (DRA), so this type was investigated further.

The DRA started out from components in microwave circuit applications being used as a high Q factor, quality factor, elements for energy storage. In [9] it was discovered that the DRA

is an efficient radiator if the shielding is removed and the proper mode is excited. The resonance with the DRA is established by the energy clashing up against the walls of the dielectric hitting it straight on and forming standing waves. There has been a large amount of research on DRAs [10, 11]. The size can be reduced by introducing metal to the design [12] and by increasing the dielectric constant of the antenna [13]. To date the thinnest dielectric antenna found in literature is [14], this antenna uses a very high dielectric constant of 1000 and has a thickness of 2.5 mm. The aim of this project is to have an all-dielectric ultra-thin antenna without using a really high dielectric constant so it was determined that for such a thin device the resonant mechanism of the DRA would not work. So a novel concept for an antenna is presented in this work utilizing total internal reflection (TIR) to excite a leaky whispering gallery mode.

Chapter 2 – Computational Electromagnetic Methods

This chapter presents the computational methods used to analyze the antenna. Finite-difference approximations where used to solve Maxwell's equations with the constitutive relations. Two methods where implemented for this project. The first was a one dimensional slab waveguide analysis which performs an analysis to find what modes exist in a slab. The second method was a two dimensional finite-difference frequency domain (FDFD) method, which solves and visualizes steady state fields. Both of these methods where implemented using MATLAB. The commercial software package ANSYS HFSS was used to perform a rigorous 3D simulation to corroborate the other simulations and finalize the design of the DPA.

2.1 MAXWELL'S EQUATIONS

We will begin by preparing Maxwell's equations for the methods [15]. Maxwell's equations in differential form in the time domain are

$$\nabla \bullet \vec{D}(t) = \rho_v(t) \tag{2.1}$$

$$\nabla \bullet \vec{B}(t) = 0 \tag{2.2}$$

$$\nabla \times \vec{H}(t) = \vec{J}(t) + \frac{\partial \vec{D}(t)}{\partial t} \tag{2.3}$$

$$\nabla \times \vec{E}(t) = -\frac{\partial \vec{B}(t)}{\partial t} \tag{2.4}$$

Here $\vec{D}$ is the electric flux density $\left(C/m^2\right)$, ρ_v is the electric charge density $\left(C/m^3\right)$, $\vec{B}$ is the magnetic flux density $\left(W/m^2\right)$, $\vec{H}$ is the magnetic field intensity $\left(A/m\right)$, $\vec{J}$ is the electric current density $\left(A/m^2\right)$, and $\vec{E}$ is the electric field intensity $\left(V/m\right)$.

The constitutive relations describe how waves interact with materials and they are the following

$$\vec{D}(t) = \left[\varepsilon(t)\right] * \vec{E}(t) \tag{2.5}$$

$$\vec{B}(t) = \left[\mu(t)\right] * \vec{H}(t) \tag{2.6}$$

Here ε is the permittivity (F/m), and μ is the permeability (H/m), these are tensors and the equations in the time domain involve convolutions.

We can convert Maxwell's equations and the constitutive relations to the frequency domain and simplify them by assuming no static charges or currents, $\rho_v = \vec{J}(t) = 0$. We will further simplify the equations by assuming linear, homogeneous and isotropic materials. This will reduce the permittivity and permeability tensors to scalars because the material properties are uniform in all directions. These assumptions will yield the following frequency domain equations

$$\nabla \bullet \vec{D} = 0 \tag{2.7}$$

$$\nabla \bullet \vec{B} = 0 \tag{2.8}$$

$$\nabla \times \vec{E} = -j\omega\vec{B} \tag{2.9}$$

$$\nabla \times \vec{H} = j\omega\vec{D} \tag{2.10}$$

$$\vec{D} = \varepsilon\vec{E} \tag{2.11}$$

$$\vec{B} = \mu\vec{H} \tag{2.12}$$

We can expand (2.11) and (2.12) by the following relationships

$$\varepsilon = \varepsilon_o\varepsilon_r \tag{2.13}$$

$$\mu = \mu_o\mu_r \tag{2.14}$$

Here ε_o is the permittivity of free space, ε_r is the relative permittivity or dielectric constant, μ_o is the permeability of free space and μ_r is the relative permeability. This yields the following for the constitutive relations

$$\vec{D} = \varepsilon_o\varepsilon_r\vec{E} \tag{2.15}$$

$$\vec{B} = \mu_o\mu_r\vec{H} \tag{2.16}$$

We can substitute equations (2.15) and (2.16) into (2.9) and (2.10) to get the following

$$\nabla \times \vec{E} = -j\omega\mu_o\mu_r\vec{H} \tag{2.17}$$

$$\nabla \times \vec{H} = j\omega\varepsilon_o\varepsilon_r\vec{E} \tag{2.18}$$

We can further simplify these equations by normalizing the magnetic field by the following equation

$$\vec{\tilde{H}} = -j\sqrt{\frac{\mu_o}{\varepsilon_o}}\vec{H} \tag{2.19}$$

This normalization also provides the benefit that the electric field and magnetic fields will be of the same magnitude during our computations and thus reduce the loss of significant digits due to truncation. The resulting equations are

$$\nabla \times \vec{E} = k_o\mu_r\vec{\tilde{H}} \tag{2.20}$$

$$\nabla \times \vec{\tilde{H}} = k_o\varepsilon_r\vec{E} \tag{2.21}$$

Where k_o is the wave number and is equal to the following

$$k_o = \omega\sqrt{\mu_o\varepsilon_o} \tag{2.22}$$

We can expand equations (2.20) and (2.21) to the following

$$\frac{\partial E_z}{\partial y} - \frac{\partial E_y}{\partial z} = k_o\mu_r\tilde{H}_x \tag{2.23}$$

$$\frac{\partial E_x}{\partial z} - \frac{\partial E_z}{\partial x} = k_o\mu_r\tilde{H}_y \tag{2.24}$$

$$\frac{\partial E_y}{\partial x} - \frac{\partial E_x}{\partial y} = k_o\mu_r\vec{\tilde{H}}_z \tag{2.25}$$

$$\frac{\partial \tilde{H}_z}{\partial y} - \frac{\partial \tilde{H}_y}{\partial z} = k_o\varepsilon_r E_x \tag{2.26}$$

$$\frac{\partial \tilde{H}_x}{\partial z} - \frac{\partial \tilde{H}_z}{\partial x} = k_o\varepsilon_r E_y \tag{2.27}$$

$$\frac{\partial \tilde{H}_y}{\partial x} - \frac{\partial \tilde{H}_x}{\partial y} = k_o\varepsilon_r E_z \tag{2.28}$$

We can further simplify (2.23)-(2.28) by normalizing the spatial coordinates according to the following

$$x' = k_o x \tag{2.29}$$

$$y' = k_o y \tag{2.30}$$

$$z' = k_o z \tag{2.31}$$

Substituting equations (2.29)-(2.31) into equations (2.23)-(2.28) will give the following

$$\frac{\partial E_z}{\partial y'} - \frac{\partial E_y}{\partial z'} = \mu_r \tilde{H}_x \tag{2.32}$$

$$\frac{\partial E_x}{\partial z'} - \frac{\partial E_z}{\partial x'} = \mu_r \tilde{H}_y \tag{2.33}$$

$$\frac{\partial E_y}{\partial x'} - \frac{\partial E_x}{\partial y'} = \mu_r \tilde{\tilde{H}}_z \tag{2.34}$$

$$\frac{\partial \tilde{H}_z}{\partial y'} - \frac{\partial \tilde{H}_y}{\partial z'} = \varepsilon_r E_x \tag{2.35}$$

$$\frac{\partial \tilde{H}_x}{\partial z'} - \frac{\partial \tilde{H}_z}{\partial x'} = \varepsilon_r E_y \tag{2.36}$$

$$\frac{\partial \tilde{H}_y}{\partial x'} - \frac{\partial \tilde{H}_x}{\partial y'} = \varepsilon_r E_z \tag{2.37}$$

These equations will be the starting point for FDFD and slab waveguide analysis.

2.2 FINITE-DIFFERENCE APPROXIMATION

Equations (2.32)-(2.37) contain first order partial derivatives. In order to compute these partial derivatives a finite-difference approximation will be used. Specifically we will be using a central finite-difference approximation [16]. The central finite-difference approximation approximates the derivative at a location by using the next and the previous points.

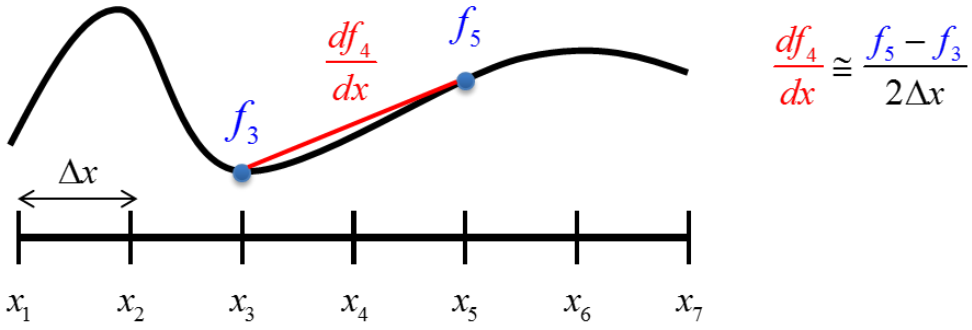

Figure 2.1: Finite-difference approximation with central finite-difference.

Figure 2.1 shows an example of the central finite-difference approximation in one dimension where

$$\frac{df_i}{dx} \cong \frac{f_{i+1} - f_{i-1}}{2\Delta x} \tag{2.38}$$

For this project we will be using Dirichlet boundary conditions [16] with the assumption that the fields outside our solution space are equal to zero.

2.3 YEE GRID

For this project the Yee grid was adopted [17, 18]. The Yee grid staggers the field components as seen in Figure 2.2. The staggering of the electric and magnetic field components according to the Yee grid yields an elegant derivation of the curl equations as well as satisfying physical boundary conditions. The Yee grid implementation is also divergence free satisfying the two divergence equations in Maxwell's equations.

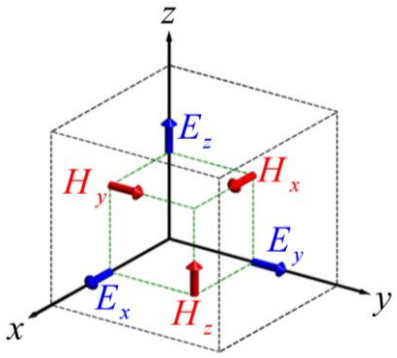

Figure 2.2: Yee grid unit cell [18].

The Yee grid does have the consequence that because the field components are staggered then the components from the same Yee cell can see different material properties.

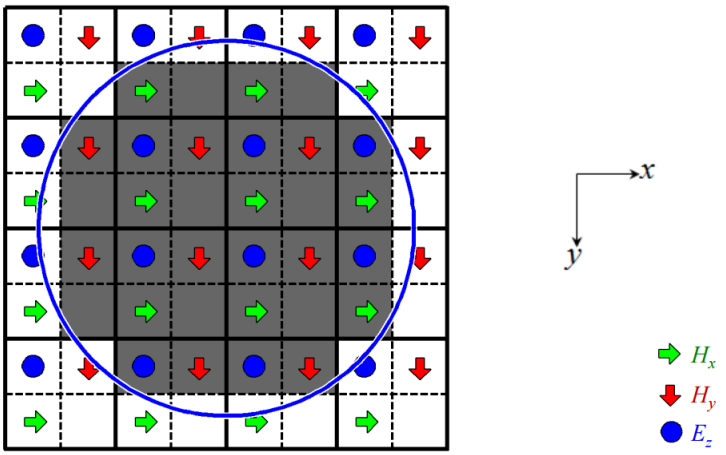

Figure 2.3: 2D grid showing the staggering of field components according to the Yee grid [19].

Figure 2.3 shows how the field components are staggered in a two dimensional solution space according to the Yee grid. The component within the same Yee cell, represented by a 2×2 cell, can see different material properties. Therefore the permittivity and permeability seen by components of the same cell can be different and thus will be represented by $\varepsilon_{xx},\varepsilon_{yy},\varepsilon_{zz},\mu_{xx},\mu_{yy},\mu_{zz}$. These quantities are not to be confused with anisotropic tensor quantities but simply represent the material properties seen by the corresponding field component. Substituting them into (2.32)-(2.37) gives

$$\frac{\partial E_z}{\partial y'}-\frac{\partial E_y}{\partial z'}=\mu_{xx}\tilde{H}_x \tag{2.39}$$

$$\frac{\partial E_x}{\partial z'}-\frac{\partial E_z}{\partial x'}=\mu_{yy}\tilde{H}_y \tag{2.40}$$

$$\frac{\partial E_y}{\partial x'}-\frac{\partial E_x}{\partial y'}=\mu_{zz}\tilde{H}_z \tag{2.41}$$

$$\frac{\partial \tilde{H}_z}{\partial y'}-\frac{\partial \tilde{H}_y}{\partial z'}=\varepsilon_{xx}E_x \tag{2.42}$$

$$\frac{\partial \tilde{H}_x}{\partial z'} - \frac{\partial \tilde{H}_z}{\partial x'} = \varepsilon_{yy} E_y \tag{2.43}$$

$$\frac{\partial \tilde{H}_y}{\partial x'} - \frac{\partial \tilde{H}_x}{\partial y'} = \varepsilon_{zz} E_z \tag{2.44}$$

So ε_{xx} is the relative permittivity seen by E_x throughout the grid, ε_{yy} is the relative permittivity seen by E_y, ε_{zz} is the relative permittivity seen by E_z, and same for the relative permeability with μ_{xx} is the relative permeability seen by H_x and so on. Using the central finite-difference approximation with the staggering of the Yee grid will give the following finite-difference approximation of the curl equations, where i, j, k are the indices for x, y, z.

$$\frac{E_z^{i,j+1,k} - E_z^{i,j,k}}{\Delta y'} - \frac{E_z^{i,j,k+1} - E_z^{i,j,k}}{\Delta z'} = \mu_{xx}^{i,j,k} \tilde{H}_x^{i,j,k} \tag{2.45}$$

$$\frac{E_x^{i,j,k+1} - E_x^{i,j,k}}{\Delta z'} - \frac{E_z^{i+1,j,k} - E_z^{i,j,k}}{\Delta x'} = \mu_{yy}^{i,j,k} \tilde{H}_y^{i,j,k} \tag{2.46}$$

$$\frac{E_y^{i+1,j,k} - E_y^{i,j,k}}{\Delta x'} - \frac{E_x^{i,j+1,k} - E_x^{i,j,k}}{\Delta y'} = \mu_{zz}^{i,j,k} \tilde{H}_z^{i,j,k} \tag{2.47}$$

$$\frac{\tilde{H}_z^{i,j,k} - \tilde{H}_z^{i,j-1,k}}{\Delta y'} - \frac{\tilde{H}_z^{i,j,k} - \tilde{H}_z^{i,j,k-1}}{\Delta z'} = \varepsilon_{xx}^{i,j,k} E_x^{i,j,k} \tag{2.48}$$

$$\frac{\tilde{H}_x^{i,j,k} - \tilde{H}_x^{i,j,k-1}}{\Delta z'} - \frac{\tilde{H}_z^{i,j,k} - \tilde{H}_z^{i-1,j,k}}{\Delta x'} = \varepsilon_{yy}^{i,j,k} E_y^{i,j,k} \tag{2.49}$$

$$\frac{\tilde{H}_y^{i,j,k} - \tilde{H}_y^{i-1,j,k}}{\Delta x'} - \frac{\tilde{H}_x^{i,j,k} - \tilde{H}_x^{i,j-1,k}}{\Delta y'} = \varepsilon_{zz}^{i,j,k} E_z^{i,j,k} \tag{2.50}$$

We can form matrix derivative operators to perform the above calculations. For the electric field a matrix derivative operators for a 2D case with 3×3 grid can be seen in Figure 2.4.

$$\boldsymbol{D}^{e}_{x'} = \frac{1}{\Delta x'}\begin{bmatrix} -1 & 1 & & & & & & & & \\ & -1 & 1 & & & & & & & \\ & & -1 & 0 & & & & & & \\ & & & -1 & 1 & & & & & \\ & & & & -1 & 1 & & & & \\ & & & & & -1 & 0 & & & \\ & & & & & & -1 & 1 & & \\ & & & & & & & -1 & 1 & \\ & & & & & & & & -1 & \end{bmatrix} \quad \boldsymbol{D}^{e}_{y'} = \frac{1}{\Delta y'}\begin{bmatrix} -1 & 0 & 0 & 1 & & & & & & \\ & -1 & 0 & 0 & 1 & & & & & \\ & & -1 & 0 & 0 & 1 & & & & \\ & & & -1 & 0 & 0 & 1 & & & \\ & & & & -1 & 0 & 0 & 1 & & \\ & & & & & -1 & 0 & 0 & 1 & \\ & & & & & & -1 & 0 & 0 & \\ & & & & & & & -1 & 0 & \\ & & & & & & & & -1 & \end{bmatrix}$$

Figure 2.4: Matrix derivative for the electric field in *x* (left), matrix derivative for the electric field in *y* (right).

For the magnetic field the matrix derivative operators for the same case can be seen in Figure 2.5.

$$\boldsymbol{D}^{h}_{x'} = \frac{1}{\Delta x'}\begin{bmatrix} 1 & & & & & & & & & \\ -1 & 1 & & & & & & & & \\ & -1 & 1 & & & & & & & \\ & & 0 & 1 & & & & & & \\ & & & -1 & 1 & & & & & \\ & & & & -1 & 1 & & & & \\ & & & & & 0 & 1 & & & \\ & & & & & & -1 & 1 & & \\ & & & & & & & -1 & 1 & \end{bmatrix} \quad \boldsymbol{D}^{h}_{y'} = \frac{1}{\Delta y'}\begin{bmatrix} 1 & & & & & & & & & \\ 0 & 1 & & & & & & & & \\ 0 & 0 & 1 & & & & & & & \\ -1 & 0 & 0 & 1 & & & & & & \\ & -1 & 0 & 0 & 1 & & & & & \\ & & -1 & 0 & 0 & 1 & & & & \\ & & & -1 & 0 & 0 & 1 & & & \\ & & & & -1 & 0 & 0 & 1 & & \\ & & & & & -1 & 0 & 0 & 1 & \end{bmatrix}$$

Figure 2.5: Matrix derivative for the electric field in *x* (left), matrix derivative for the electric field in *y* (right).

2.4 SLAB WAVEGUIDE ANALYSIS

The first method is a finite-difference analysis of a slab waveguide [20]. The slab waveguide analysis is a one dimensional analysis in which the y and z directions are assumed to be uniform and propagation is restricted to the *z* direction.

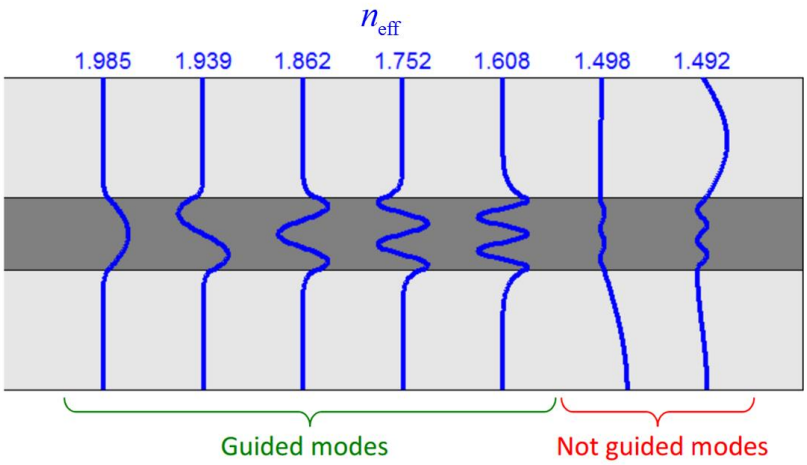

Figure 2.6: Slab waveguide analysis example [20].

Figure 2.6 shows an example of a slab waveguide analysis and the output generated. The guided modes are confined in the slab and decay to zero, the non-guided modes are from the simulation itself where the solution space is seen as a waveguide. First to perform the slab waveguide analysis we assume the form for a solution for a mode in a waveguide to be.

$$\vec{E}(x,y,z) = \vec{A}(x,y)e^{-\tilde{\gamma}z} \tag{2.51}$$

$$\vec{\tilde{H}}(x,y,z) = \vec{B}(x,y)e^{-\tilde{\gamma}z} \tag{2.52}$$

Here $\vec{A}$ and $\vec{B}$ are the complex amplitudes of the mode, and $\tilde{\gamma}$ is the complex propagation constant normalized by the wave number k_o, $\tilde{\gamma}$ contains information about attenuation and oscillation. The complex propagation constant also has the following relationship with the effective refractive index, n_{eff}.

$$\tilde{\gamma} = jn_{\text{eff}} \tag{2.53}$$

Next we will substitute the solutions (2.51) and (2.52) into the curl equations (2.39)-(2.44) which yields the following

$$\frac{\partial A_z}{\partial y'} + \tilde{\gamma}A_y = \mu_{xx}B_x \tag{2.54}$$

$$-\tilde{\gamma}A_x - \frac{\partial A_z}{\partial x'} = \mu_{yy}B_y \tag{2.55}$$

$$\frac{\partial A_y}{\partial x'} - \frac{\partial A_x}{\partial y'} = \mu_{zz} B_z \tag{2.56}$$

$$\frac{\partial B_z}{\partial y'} + \tilde{\gamma} B_y = \varepsilon_{xx} A_x \tag{2.57}$$

$$-\tilde{\gamma} B_x - \frac{\partial B_z}{\partial x'} = \varepsilon_{yy} A_y \tag{2.58}$$

$$\frac{\partial B_y}{\partial x'} - \frac{\partial B_x}{\partial y'} = \varepsilon_{zz} A_z \tag{2.59}$$

The above equations can be written in matrix form and give the following

$$\boldsymbol{D}_{y'}^{e} \boldsymbol{a}_z + \tilde{\gamma} \boldsymbol{a}_y = \boldsymbol{\mu}_{xx} \boldsymbol{b}_x \tag{2.60}$$

$$-\tilde{\gamma} \boldsymbol{a}_x - \boldsymbol{D}_{x'}^{e} \boldsymbol{a}_z = \boldsymbol{\mu}_{yy} \boldsymbol{b}_y \tag{2.61}$$

$$\boldsymbol{D}_{x'}^{e} \boldsymbol{a}_y - \boldsymbol{D}_{y'}^{e} \boldsymbol{a}_x = \boldsymbol{\mu}_{zz} \boldsymbol{b}_z \tag{2.62}$$

$$\boldsymbol{D}_{y'}^{h} \boldsymbol{b}_z + \tilde{\gamma} \boldsymbol{b}_y = \boldsymbol{\varepsilon}_{xx} \boldsymbol{a}_x \tag{2.63}$$

$$-\tilde{\gamma} \boldsymbol{b}_x - \boldsymbol{D}_{x'}^{h} \boldsymbol{b}_z = \boldsymbol{\varepsilon}_{yy} \boldsymbol{a}_y \tag{2.64}$$

$$\boldsymbol{D}_{x'}^{h} \boldsymbol{b}_y - \boldsymbol{D}_{y'}^{h} \boldsymbol{b}_x = \boldsymbol{\varepsilon}_{zz} \boldsymbol{a}_z \tag{2.65}$$

Now we can reduce the above equations for a one dimensional analysis by assuming the y direction is uniform and it will result in the following

$$\cancel{\boldsymbol{D}_{y'}^{e} \boldsymbol{a}_z} + \tilde{\gamma} \boldsymbol{a}_y = \boldsymbol{\mu}_{xx} \boldsymbol{b}_x \tag{2.66}$$

$$-\tilde{\gamma} \boldsymbol{a}_x - \boldsymbol{D}_{x'}^{e} \boldsymbol{a}_z = \boldsymbol{\mu}_{yy} \boldsymbol{b}_y \tag{2.67}$$

$$\boldsymbol{D}_{x'}^{e} \boldsymbol{a}_y - \cancel{\boldsymbol{D}_{y'}^{e} \boldsymbol{a}_x} = \boldsymbol{\mu}_{zz} \boldsymbol{b}_z \tag{2.68}$$

$$\cancel{\boldsymbol{D}_{y'}^{h} \boldsymbol{b}_z} + \tilde{\gamma} \boldsymbol{b}_y = \boldsymbol{\varepsilon}_{xx} \boldsymbol{a}_x \tag{2.69}$$

$$-\tilde{\gamma} \boldsymbol{b}_x - \boldsymbol{D}_{x'}^{h} \boldsymbol{b}_z = \boldsymbol{\varepsilon}_{yy} \boldsymbol{a}_y \tag{2.70}$$

$$\boldsymbol{D}_{x'}^{h} \boldsymbol{b}_y - \cancel{\boldsymbol{D}_{y'}^{h} \boldsymbol{b}_x} = \boldsymbol{\varepsilon}_{zz} \boldsymbol{a}_z \tag{2.71}$$

The equations decouple into two distinct polarizations which we will refer to as the horizontal polarization, this will have the electric field polarized in the $x-y$ plane of the antenna, and the vertical polarization which will have the electric field polarized perpendicular to the $x-y$ plane of the antenna. We can rearrange the equations into the two different polarizations yielding for the horizontal polarization

$$\tilde{\gamma}\boldsymbol{a}_y = \boldsymbol{\mu}_{xx}\boldsymbol{b}_x \tag{2.72}$$

$$\boldsymbol{D}_{x'}^{e}\boldsymbol{a}_y = \boldsymbol{\mu}_{zz}\boldsymbol{b}_z \tag{2.73}$$

$$-\tilde{\gamma}\boldsymbol{b}_x - \boldsymbol{D}_{x'}^{h}\boldsymbol{b}_z = \boldsymbol{\varepsilon}_{yy}\boldsymbol{a}_y \tag{2.74}$$

For the vertical polarization we have

$$\tilde{\gamma}\boldsymbol{b}_y = \boldsymbol{\varepsilon}_{xx}\boldsymbol{a}_x \tag{2.75}$$

$$\boldsymbol{D}_{x'}^{h}\boldsymbol{b}_y = \boldsymbol{\varepsilon}_{zz}\boldsymbol{a}_z \tag{2.76}$$

$$-\tilde{\gamma}\boldsymbol{a}_x - \boldsymbol{D}_{x'}^{e}\boldsymbol{a}_z = \boldsymbol{\mu}_{yy}\boldsymbol{b}_y \tag{2.77}$$

We can solve these systems of equations and have the following for the horizontal polarization

$$-\left(\boldsymbol{D}_{x'}^{e}\boldsymbol{\mu}_{xx}^{-1}\boldsymbol{D}_{x'}^{h} + \boldsymbol{\varepsilon}_{yy}\right)\boldsymbol{a}_y = \tilde{\gamma}^2\boldsymbol{\mu}_{xx}^{-1}\boldsymbol{a}_y \tag{2.78}$$

Similarly solving the equations for the vertical polarization gives

$$-\left(\boldsymbol{D}_{x'}^{e}\boldsymbol{\varepsilon}_{xx}^{-1}\boldsymbol{D}_{x'}^{h} + \boldsymbol{\mu}_{yy}\right)\boldsymbol{b}_y = \tilde{\gamma}^2\boldsymbol{\varepsilon}_{xx}^{-1}\boldsymbol{b}_y \tag{2.79}$$

Equations (2.78) and (2.79) are in the form of a generalized eigen-value problem

$$\boldsymbol{A}\boldsymbol{x} = \lambda\boldsymbol{B}\boldsymbol{x} \tag{2.80}$$

Solving (2.78) and (2.79) will yield solutions representing the modes like in Figure 2.6 for each of the two polarizations.

2.5 FINITE-DIFFERENCE FREQUENCY DOMAIN METHOD

The second method used is FDFD. A two dimensional simulation using the FDFD method was performed to visualize the steady state fields. This method will start with equations (2.39)-(2.44). To reduce the problem to a two dimensional simulation the z direction will be assumed uniform and propagation will be restricted to the x-y plane. This yields the following reduction

$$\frac{\partial E_z}{\partial y'} - \cancel{\frac{\partial E_y}{\partial z'}} = \mu_{xx}\tilde{H}_x \tag{2.81}$$

$$\cancel{\frac{\partial E_x}{\partial z'}} - \frac{\partial E_z}{\partial x'} = \mu_{yy}\tilde{H}_y \tag{2.82}$$

$$\frac{\partial E_y}{\partial x'} - \frac{\partial E_x}{\partial y'} = \mu_{zz}\tilde{H}_z \tag{2.83}$$

$$\frac{\partial \tilde{H}_z}{\partial y'} - \cancel{\frac{\partial \tilde{H}_y}{\partial z'}} = \varepsilon_{xx}E_x \tag{2.84}$$

$$\cancel{\frac{\partial \tilde{H}_x}{\partial z'}} - \frac{\partial \tilde{H}_z}{\partial x'} = \varepsilon_{yy}E_y \tag{2.85}$$

$$\frac{\partial \tilde{H}_y}{\partial x'} - \frac{\partial \tilde{H}_x}{\partial y'} = \varepsilon_{zz}E_z \tag{2.86}$$

Once again the equations decouple into two different polarizations

$$\frac{\partial E_z}{\partial y'} = \mu_{xx}\tilde{H}_x \tag{2.87}$$

$$-\frac{\partial E_z}{\partial x'} = \mu_{yy}\tilde{H}_y \tag{2.88}$$

$$\frac{\partial E_y}{\partial x'} - \frac{\partial E_x}{\partial y'} = \mu_{zz}\tilde{H}_z \tag{2.89}$$

$$\frac{\partial \tilde{H}_z}{\partial y'} = \varepsilon_{xx}E_x \tag{2.90}$$

$$-\frac{\partial \tilde{H}_z}{\partial x'} = \varepsilon_{yy}E_y \tag{2.91}$$

$$\frac{\partial \tilde{H}_y}{\partial x'} - \frac{\partial \tilde{H}_x}{\partial y'} = \varepsilon_{zz}E_z \tag{2.92}$$

For the purposes of this project we are only interested in the horizontal polarization, this will be discussed later. The equations for the horizontal polarization in matrix form are

$$\boldsymbol{D}_{y'}^{h}\boldsymbol{h}_z = \boldsymbol{\varepsilon}_{xx}\boldsymbol{e}_x \tag{2.93}$$

$$-\boldsymbol{D}_{x'}^{h}\boldsymbol{h}_z = \boldsymbol{\varepsilon}_{yy}\boldsymbol{e}_y \tag{2.94}$$

$$\boldsymbol{D}_{x'}^{e}\boldsymbol{e}_y - \boldsymbol{D}_{y'}^{e}\boldsymbol{e}_x = \boldsymbol{\mu}_{zz}\boldsymbol{h}_z \tag{2.95}$$

Next we can solve this system of equations and get the following

$$\left(\boldsymbol{D}_{x'}^{e}\boldsymbol{\varepsilon}_{yy}^{-1}\boldsymbol{D}_{x'}^{h} + \boldsymbol{D}_{y'}^{e}\boldsymbol{\varepsilon}_{xx}^{-1}\boldsymbol{D}_{y'}^{h} + \boldsymbol{\mu}_{zz}\right)\boldsymbol{h}_z = 0 \tag{2.96}$$

The following is defined

$$\boldsymbol{D}_{x'}^{e}\boldsymbol{\varepsilon}_{yy}^{-1}\boldsymbol{D}_{x'}^{h} + \boldsymbol{D}_{y'}^{e}\boldsymbol{\varepsilon}_{xx}^{-1}\boldsymbol{D}_{y'}^{h} + \boldsymbol{\mu}_{zz} = \boldsymbol{A} \tag{2.97}$$

Equation (2.96) is of the form $\boldsymbol{A}\boldsymbol{x} = 0$, where x is $\tilde{\boldsymbol{h}}_z$, this yields a trivial solution and so a source is required. We will be using a Gaussian beam source which has the following form, f_{src}

$$f_{src}(x, y) = \mathrm{e}^{(-2y/w)^2}\,\mathrm{e}^{(-jk_o nx)} \tag{2.98}$$

In the above w controls the width of the beam and n is the refractive index of the medium in which the source is launched. The Gaussian beam source can be seen in Figure 2.7

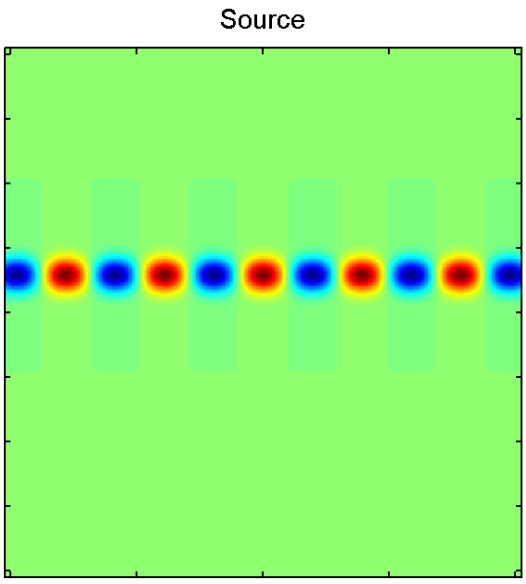

Figure 2.7: Gaussian beam source

In order to incorporate the source into equation (2.96) the total-field/scattered-field framework will be used [21]. This framework will launch a one way source by utilizing a masking matrix **Q**. Figure 2.8 shows an example of how the masking matrix is formed.

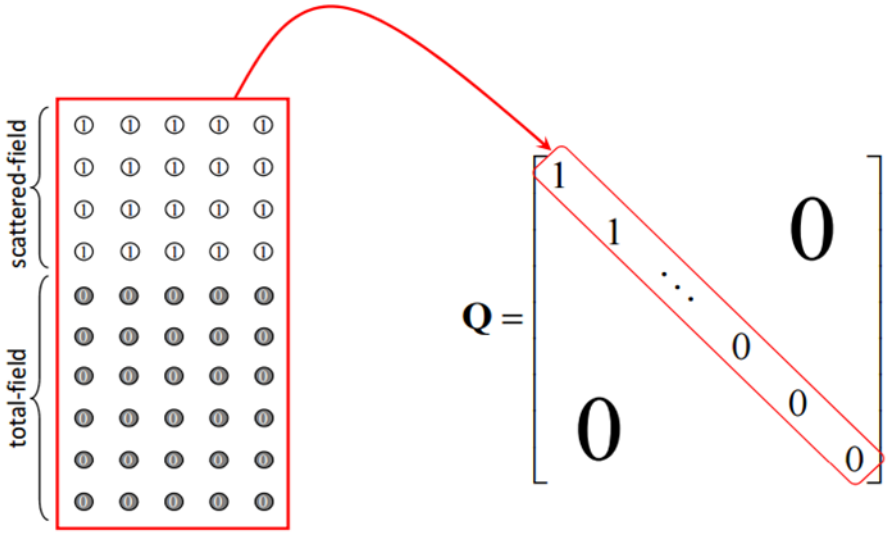

Figure 2.8: Total-field/scattered-field framework [19].

The framework requires some terms to be corrected because terms from the total-field are not wanted in the scattered-field and vice versa. So the QAAQ equation is used to form the source vector **b** where

$$\mathbf{b} = (\mathbf{QA} - \mathbf{AQ})\mathbf{f}_{src} \tag{2.99}$$

Now our equation is

$$\boldsymbol{A}\tilde{\boldsymbol{h}}_z = \boldsymbol{b} \tag{2.100}$$

We can solve for the field component $\tilde{\boldsymbol{h}}_z$ and have

$$\tilde{\boldsymbol{h}}_z = \boldsymbol{A}^{-1}\boldsymbol{b} \tag{2.101}$$

The field component can be visualized to view the steady-state fields.

In order to prevent reflections from the boundaries a uniaxial perfectly matched layer (UPML) was implemented [22, 23]. The UPML is incorporated and placed near the boundary typically starting 20 points before the boundary.

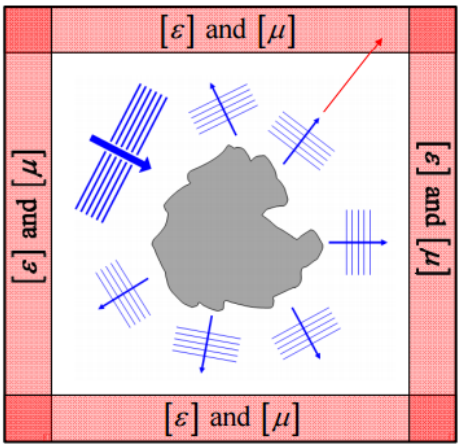

Figure 2.9: UPML in the solution space to prevent reflections from the boundaries [23].

Figure 2.9 shows the UPML near the edges of the solution space. The UPML introduces loss so that waves will decay in that region while perfectly matching the impedance regardless of

polarization, frequency or angle of incidence. The UPML will emulate the waves going off to infinity and not reflect at the boundary and interfere with the area of interest around the device.

Chapter 3: Dielectric Prism Antenna

3.1 DESIGN

The DPA was designed in stages of increasing complexity following the block diagram shown in Figure 3.1

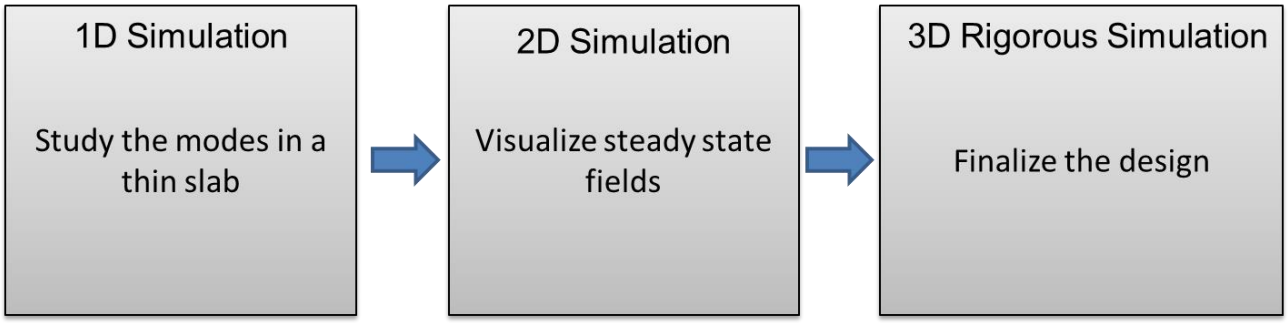

Figure 3.1:Design flow for the DPA.

So first a study of a thin slab was performed using slab waveguide analysis. The relative permittivity chosen was $\varepsilon_r = 20$ and the thickness of the slab studied was 2.5 mm. The slab was surrounded by air and the analysis found two modes which can be seen in Figure 3.2

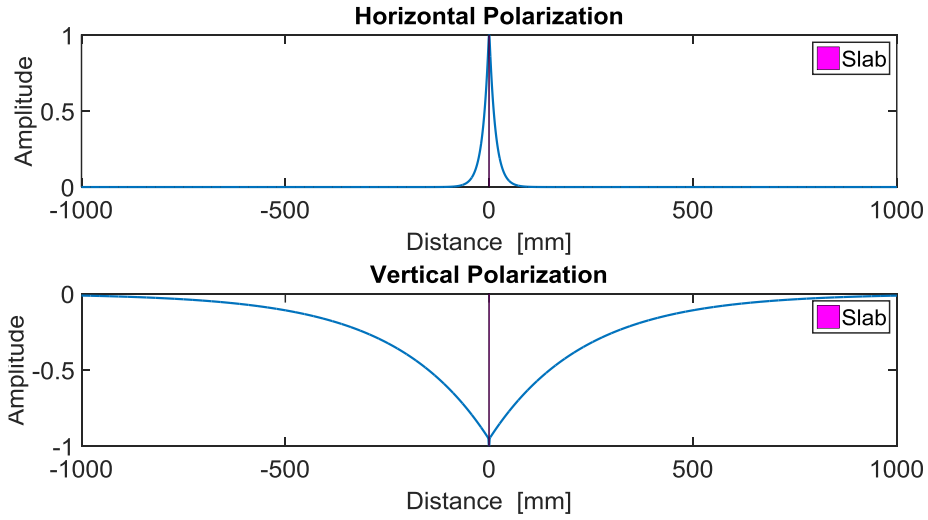

Figure 3.2: Guided modes from the slab waveguide analysis, horizontal polarization (top), vertical polarization (bottom).

Two fundamental modes where found, one for the horizontal polarization and one for the vertical polarization. The vertical polarization was larger by than the horizontal by a factor of 10λ, where λ is the free space wavelength. Choosing the vertical polarization is not a practical choice for a few reasons. First the mode is very large which would make the device very sensitive to components in proximity. Secondly it provides a lower effective refractive index, $n_{\text{eff}} = 1.003$, which results in no TIR. So the vertical polarization was chosen because the mode is well confined to the DPA and results in an effective refractive index of $n_{\text{eff}} = 1.6$. A higher effective refractive index is desired because it would make the conditions for TIR more attainable. TIR occurs above a critical angle which is governed by the equation

$$\theta_c = \sin^{-1}\left(\frac{n_1}{n_2}\right) \tag{3.1}$$

Where θ_c is the critical angle, at larger angles than the critical angle TIR will occur. The refractive index, n_1, is air in our case and n_2 is the effective refractive index calculated. Plugging in the values into (3.1) yields that the critical angle is $38.7°$.

The next step in the design now that a guided mode was found and chosen was to do a two dimensional simulation. The two dimensional simulation would study if TIR is indeed occurring.

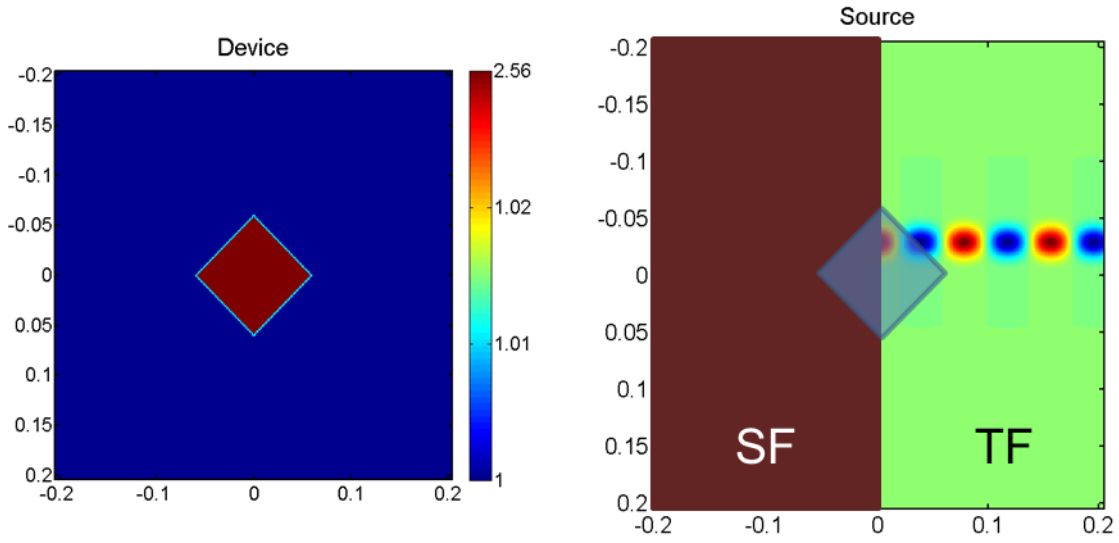

Figure 3.3: Setup used for FDFD, (left) the device, (right) the source.

Figure 3.3 shows the setup used for the FDFD simulation, the device has a side length of 7.14 cm and a thickness of 2.2 mm. The device is seen on the left and the source being injected from inside the device on the right. This simulation was performed to find if indeed TIR would happen and the device would resonate.

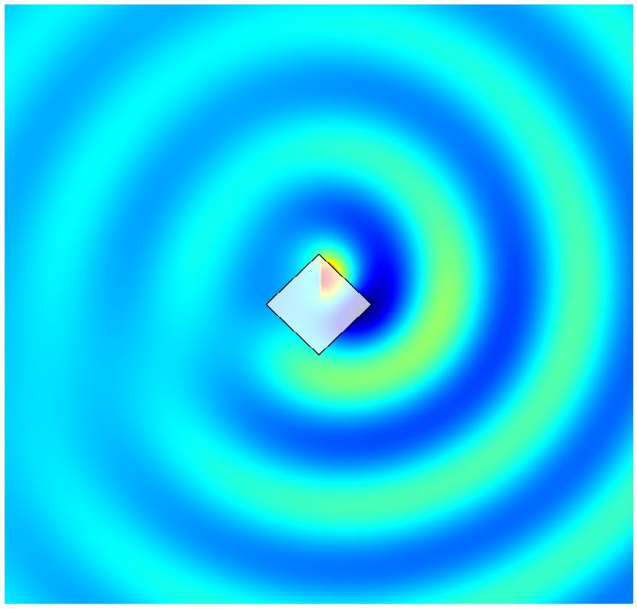

Figure 3.4:Resulting fields from the first studied device with FDFD.

In Figure 3.4 the steady-state fields are visualized and it can be seen that indeed TIR is occurring and the device is resonating. This device acts like an optical prism and therefore is being called the dielectric prism antenna. It is desired to amplify the reflections that occur in the device and this is done by increasing the angle of incidence. If the geometry is changed to increase the angle of incidence eventually the geometry converges to a circular geometry as seen in Figure 3.5.

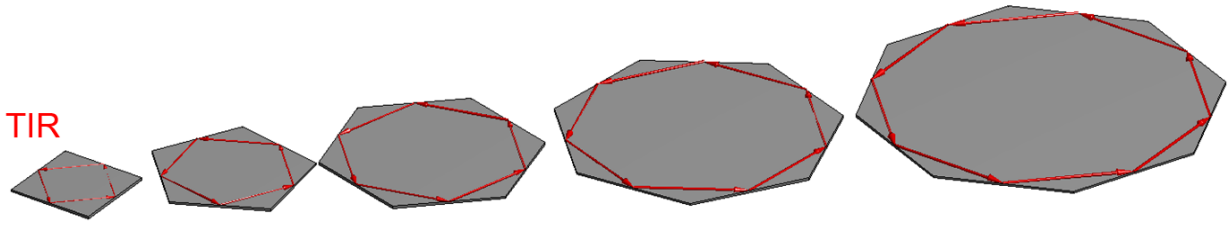

Figure 3.5: Changing the geometry to increase the angle of incidence leads to a circular design.

Having a larger angle of incidence will lead to a thinner device but also has the drawback that the device must be larger. The circular device was also studied using FDFD.

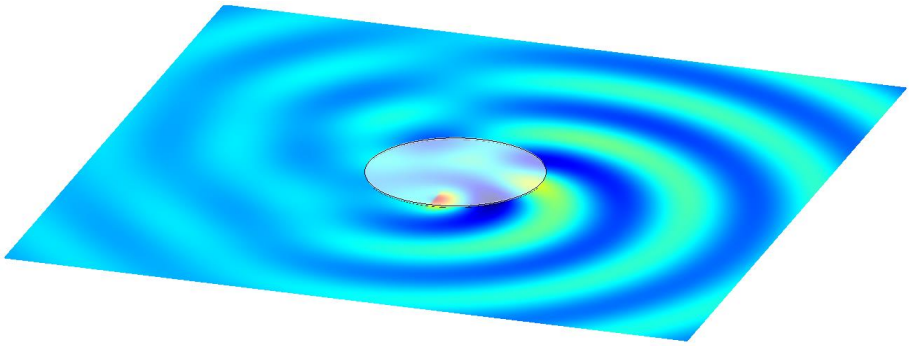

Figure 3.6: Steady-state fields of circular device.

Figure 3.6 shows the resulting fields from a FDFD simulation. The circular device was studied by sweeping both its diameter and thickness. A Gaussian beam source was launched from the top of the device in order to excite a leaky whispering gallery mode. It was found that the thickness could be decreased at the cost of increasing the diameter.

Before we move on to the rigorous simulation two things must be addressed. The first is that because the relative permittivity is equal to 20 then fully 3D printing the antenna is not currently possible in our laboratory. So instead a proof of concept implementation was done using high-ε powder from Laird Technologies.

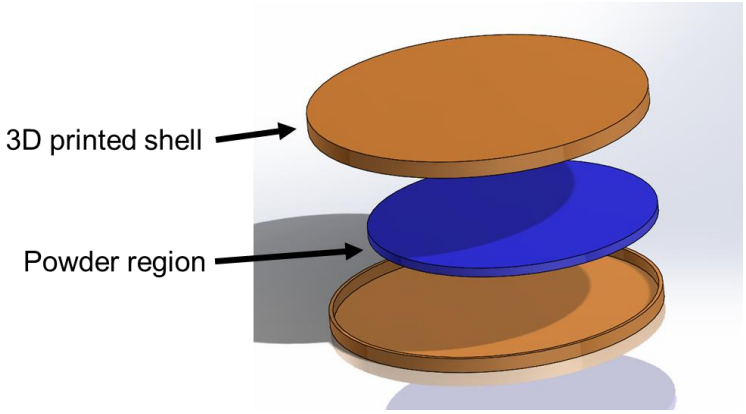

Figure 3.7: Exploded view of the antenna with the powder implementation.

Figure 3.7 shows an exploded view of the implementation performed in this project. A 3D printed shell will be packed with dielectric powder and then sealed.

The second thing that needs to be addressed now that a geometry and polarization for the antenna have been chosen is how to realistically feed it.

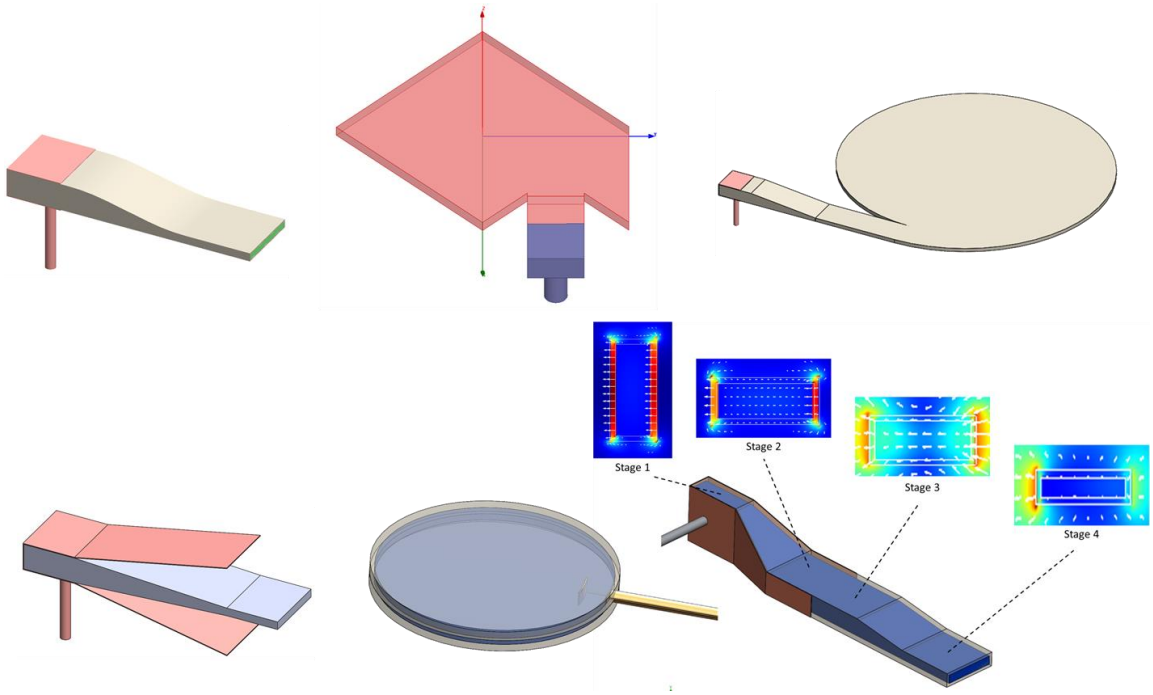

Figure 3.8: Feed concepts for the DPA.

Figure 3.8 shows various feed concepts for the DPA. Originally the idea was to launch a mode from a coaxial cable and transition it by tapering into the antenna. This proved more difficult than expected in order to match polarization and would ultimately lead to a feeding mechanism much larger than the antenna. The feed mechanism implemented in this project is a vee dipole.

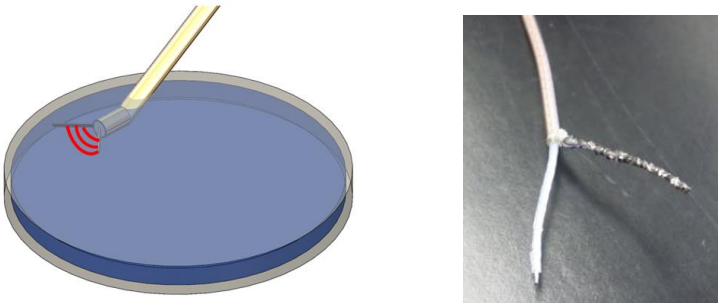

Figure 3.9: Vee dipole feed made from splitting a coaxial cable [24].

Figure 3.9 shows the vee dipole feed. This feed mechanism was chosen because it can be easy to implement and it can produce a horizontal polarization.

Next the DPA and the feed where studied in HFSS. First, the feed placement was studied because experimentally placing the feed inside the DPA would be tedious. Every time an adjustment had to be made the device would have to be destroyed and a new one made.

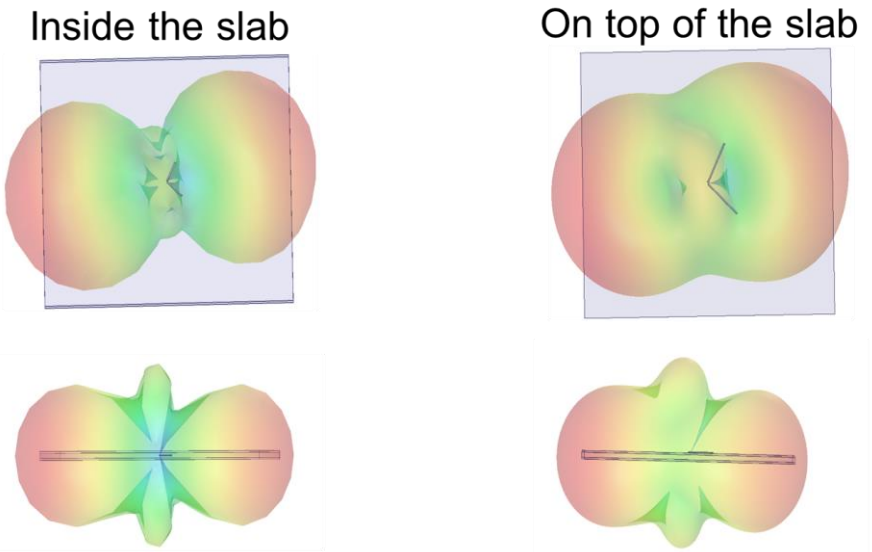

Figure 3.10: HFSS study of the feed placement.

Figure 3.10 shows the results of the radiation pattern for the study of the feed placement. On the left the feed was placed on the inside of the slab while on the right the feed was placed on top of a slab. It can be seen that the field still couples in a similar way when the feed is placed on top of the slab. The tradeoff would be less performance because the field does fringe with the

placement on top but will suffice for our purposes. Choosing the feed on top of the slab makes the experimental process easier.

Next a fully rigorous 3D simulation was performed in HFSS taking all the elements into account as can be seen in Figure 3.11.

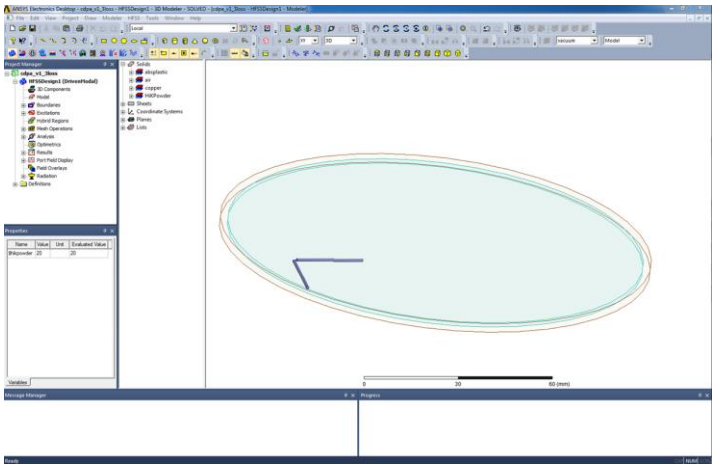

Figure 3.11: HFSS model for DPA simulation.

The impact of the thickness and diameter was also studied in HFSS.

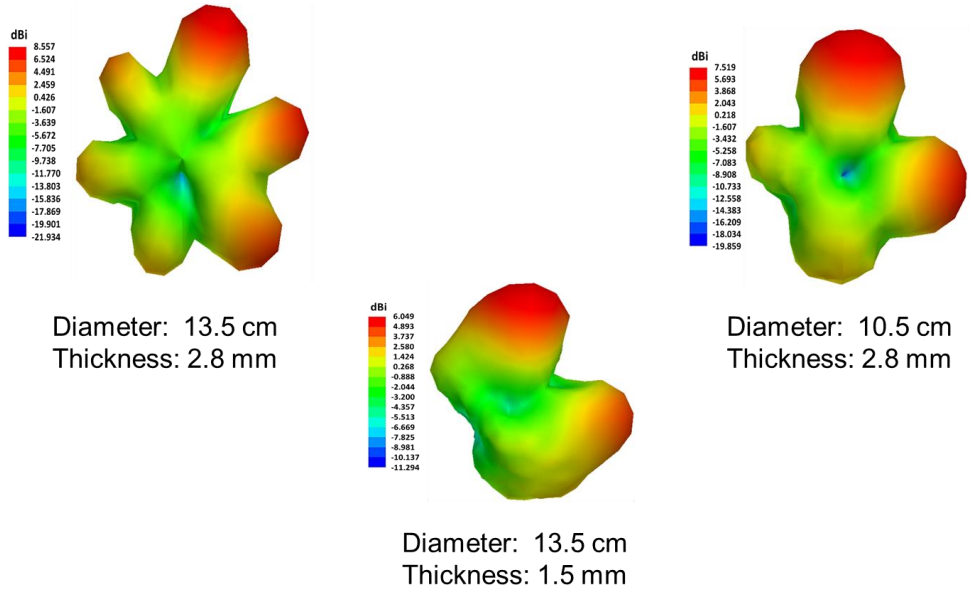

Figure 3.12: Study of the impact of thickness and diameter on the radiation pattern [24].

It was found as can be seen in Figure 3.12 that the DPA has a radiation pattern with several side lobes. The DPA with a diameter of 13.5 cm and a thickness of 2.8 mm has 6 lobes. It is believed that with the current feed mechanism a perfectly circulating mode has not yet been achieved and therefore discrete bounces are occurring and causing the radiation pattern to not appear as was expected, a smooth conch shell. Decreasing the diameter was found to decrease the lobes in the pattern further pointing to the discrete bounces happening. Finally, the thickness was decreased to see what the minimum achievable device is and it was 1.5 mm. The antenna efficiency was also studied in simulation.

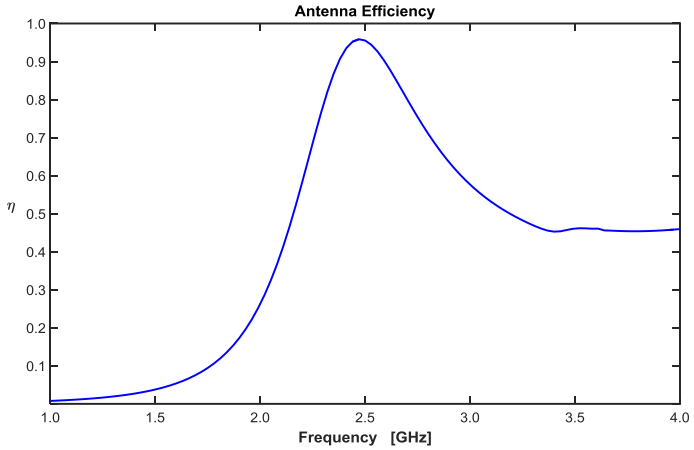

Figure 3.13: HFSS study of antenna efficiency.

Figure 3.13 shows the results obtained in simulation for the DPA with 1.5 mm. The DPA was found to have an efficiency of 95% on resonance. This was to be expected because the DPA has low loss dielectrics and few conductor losses because the only metal is the feed.

3.2 MANUFACTURING

Two DPAs where chosen to be manufactured. Both with a diameter of 13.5 cm and thicknesses of 2.8 mm, to prove the concept, and 1.5 mm, to build the thinnest possible. The manufacturing process for the DPA followed the following steps.

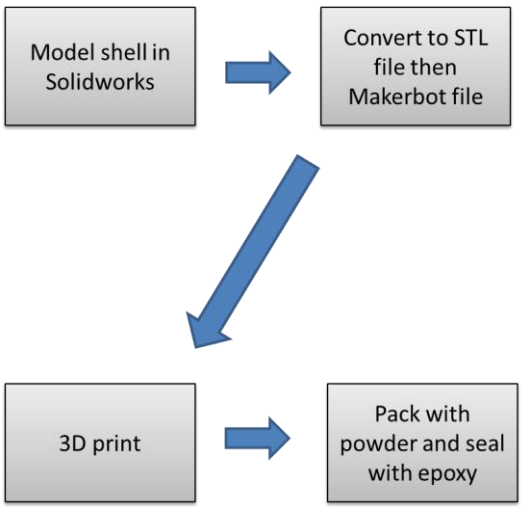

Figure 3.14: Steps of the manufacturing of the DPA.

Figure 3.14 shows the steps for manufacturing. First a shell was modeled using Solidworks, a top lid and a bottom lid which can be seen in Figure 3.15. The thickness of the shell was 1.1 mm.

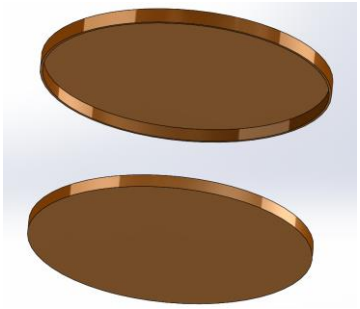

Figure 3.15: Shell modeled in Solidworks.

Then the model was converted into a STL file, then using the Makerbot software converted into instructions for printing. The 3D printer used to print the shell is the EM Lab's Makerbot Replicator 2X.

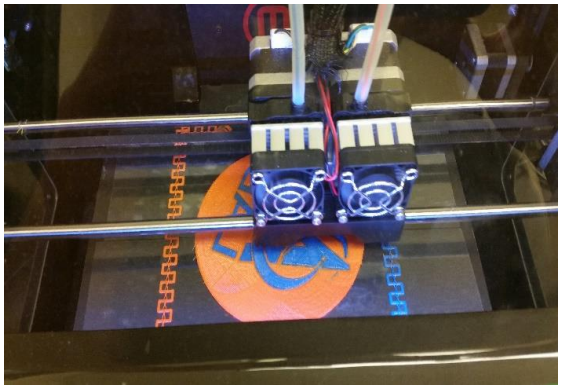

Figure 3.16: 3D printer in the process of printing the top lid [24].

Figure 3.16 shows a top lid of the shell in the process of being 3D printed. The next step is to pack the shell with powder and seal it with epoxy.

Figure 3.17: DPA shell being packed with dielectric powder (left), DPA sealed with epoxy (right) [24].

Figure 3.17 shows the DPA shell as it is being packed with dielectric powder and sealed with epoxy. The last thing that will be discussed for the manufacturing process is the final shell design. The first DPA constructed was problematic because it was not reproducing results. It was found that the powder was bulging at the center because the lids where flimsy. In order to fix this a new shell designed was implemented.

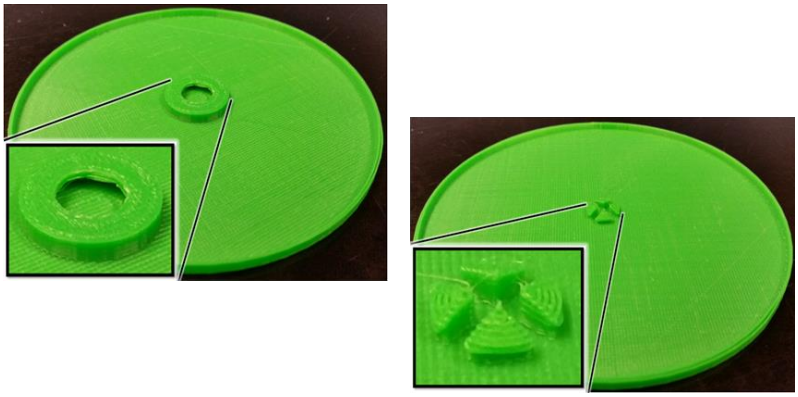

Figure 3.18: Snap lid design for DPA implementation [24].

Figure 3.18 shows the snap lid design for the DPA shell. This would make sure the packed powder stayed in place and no bulging at the center occurred. The final design for the DPA can be seen after being manufactured in Figure 3.19.

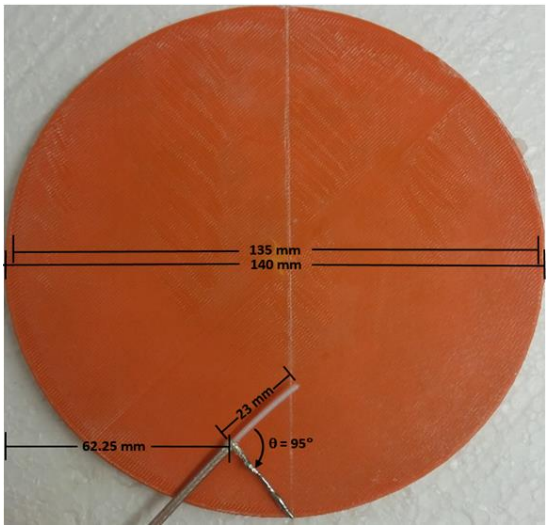

Figure 3.19: Manufactured DPA with dimensions [24].

3.3 TESTING

The DPAs that where manufactured where tested for their reflectance, S_{11}, using a vector network analyzer (VNA). This process measures how much power from port 1 is reflected back into port 1. A simple block diagram of this process can be seen in Figure 3.20.

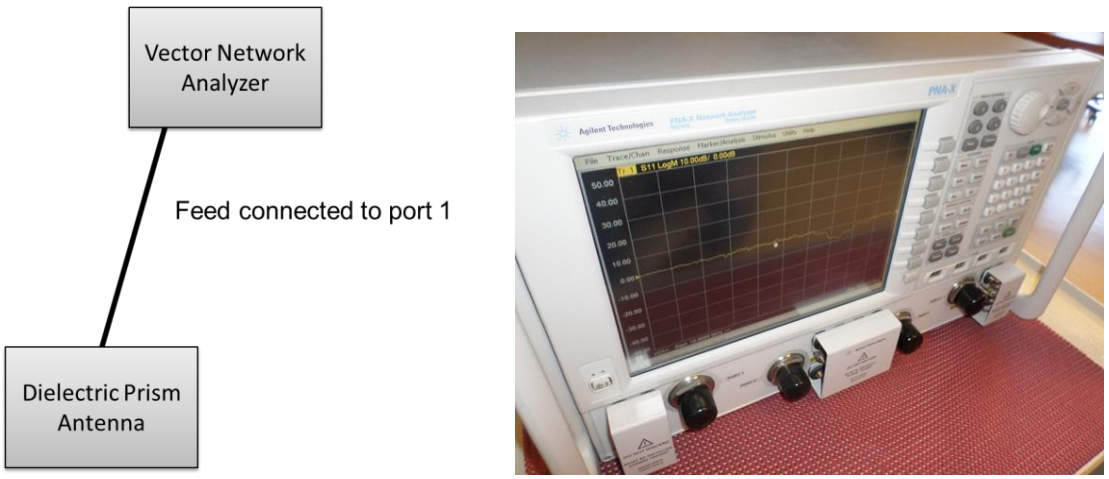

Figure 3.20:Block diagram of reflectance test (left), VNA used for testing (right).

The radiation pattern of the DPA was also tested and a block diagram can be seen in the next figure.

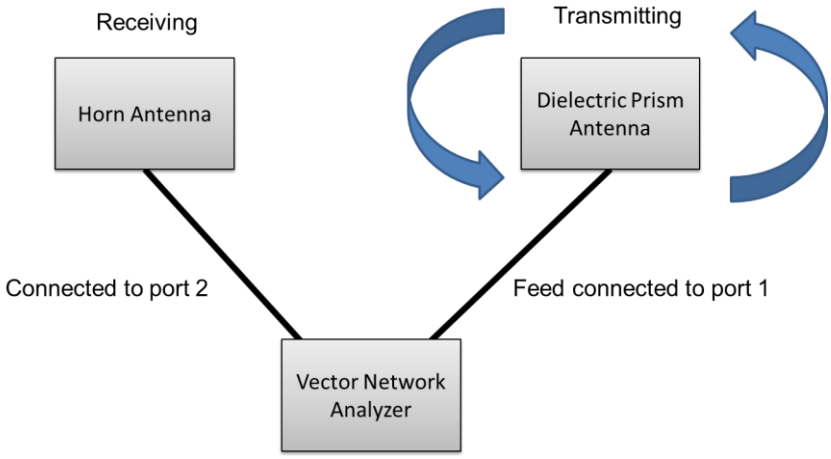

Figure 3.21:Block diagram for the radiation pattern test.

Figure 3.21 shows a block diagram for the radiation pattern test. A horn antenna, connected to port 2 of the VNA, was setup to receive and capture the horizontal polarization. If the horn antenna was setup to capture the vertical polarization then no signal would be received. The DPA, connected to port 1, was setup to transmit. Measurements were taken and the DPA was rotated every 10° until a full rotation was made. Then the data was normalized and plotted.

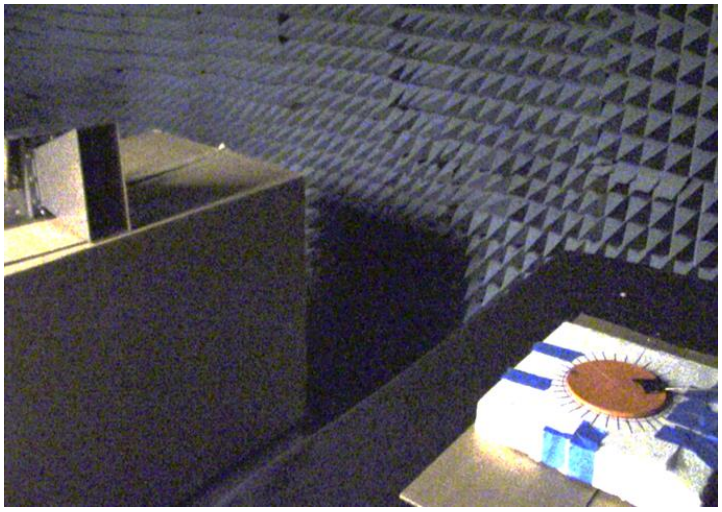

Figure 3.22: Picture of the setup for the radiation pattern testing.

Figure 3.22 shows a picture of the setup for the radiation pattern testing. The testing was performed in the UTEP EM lab's chamber.

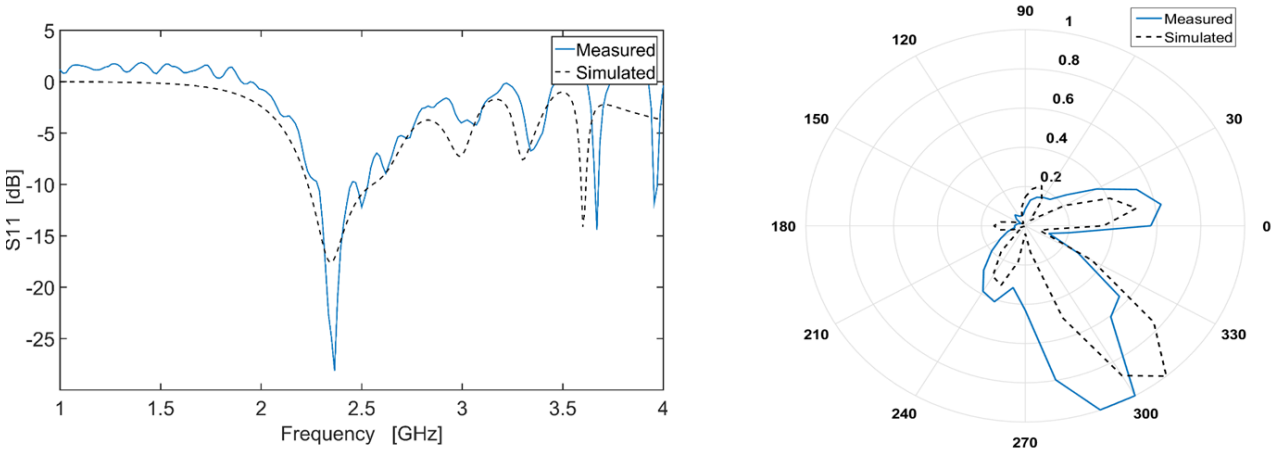

Figure 3.23: DPA with thickness of 2.8 mm S_{11} comparison of simulated and measured data (left), normalized radiation pattern comparison of simulated and measured data (right).

Figure 3.23 shows the results for the DPA with a thickness of 2.8 mm. The antenna resonates at 2.4 GHz and there is good agreement between the simulated and measured data. As can be seen in the radiation pattern a direction exists where more energy leaks out in comparison.

The thinner DPA also had good agreement between the measured and simulated results and can be seen in Figure 3.24.

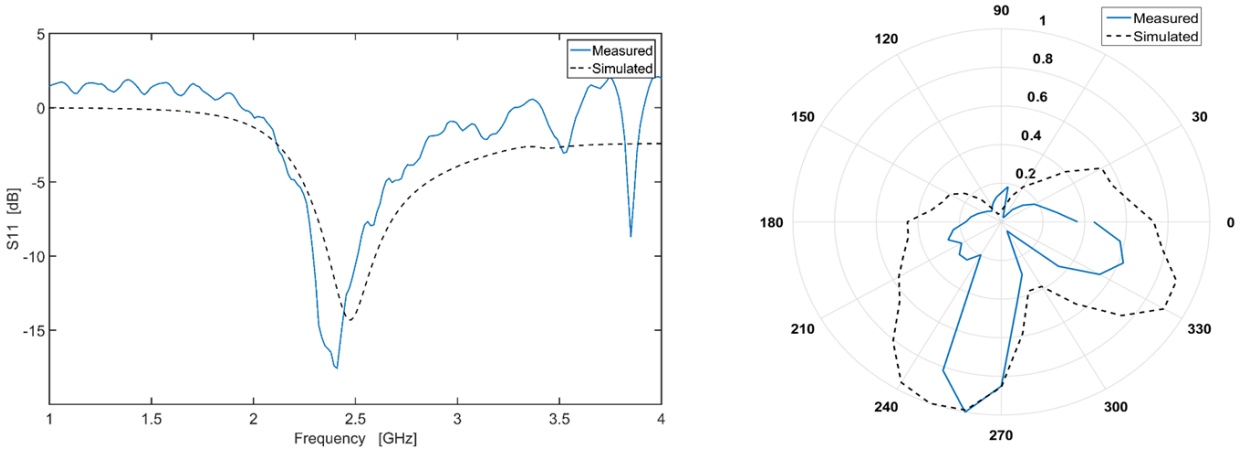

Figure 3.24:DPA with thickness of 1.5 mm S_{11} comparison of simulated and measured data (left), normalized radiation pattern comparison of simulated and measured data (right).

It is believed that because the radiation pattern testing was done by manually rotating the antenna then the measured data looks a bit different from the simulated data but it is still very closely matched.

The last test performed on the thinner DPA, thickness of 1.5 mm, was a WiFi test. A block diagram for the setup can be seen in Figure 3.25.

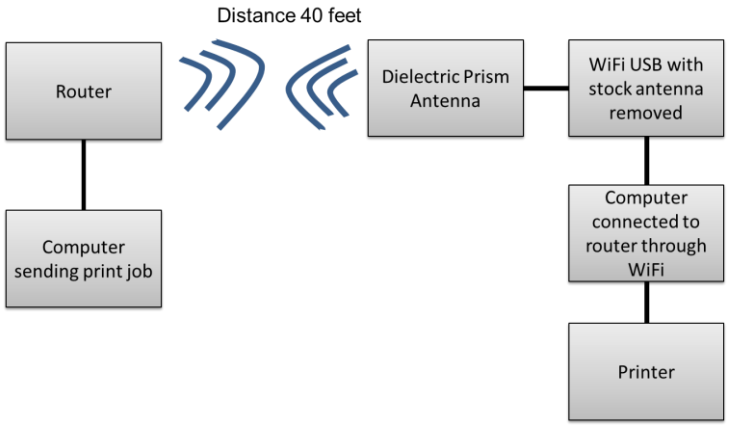

Figure 3.25:Block diagram for the WiFi test.

The DPA was setup to replace a stock monopole antenna on a USB WiFi adapter to test if the DPA would receive a print job submitted wirelessly. This test verified if the DPA would work at the WiFi frequency of 2.4 GHz. The print test was successful and the range was 40 feet. Further distances where not explored and 40 feet was chosen because it was the furthest distance in the lab. Figure 3.26 shows a picture of the whole setup at close range.

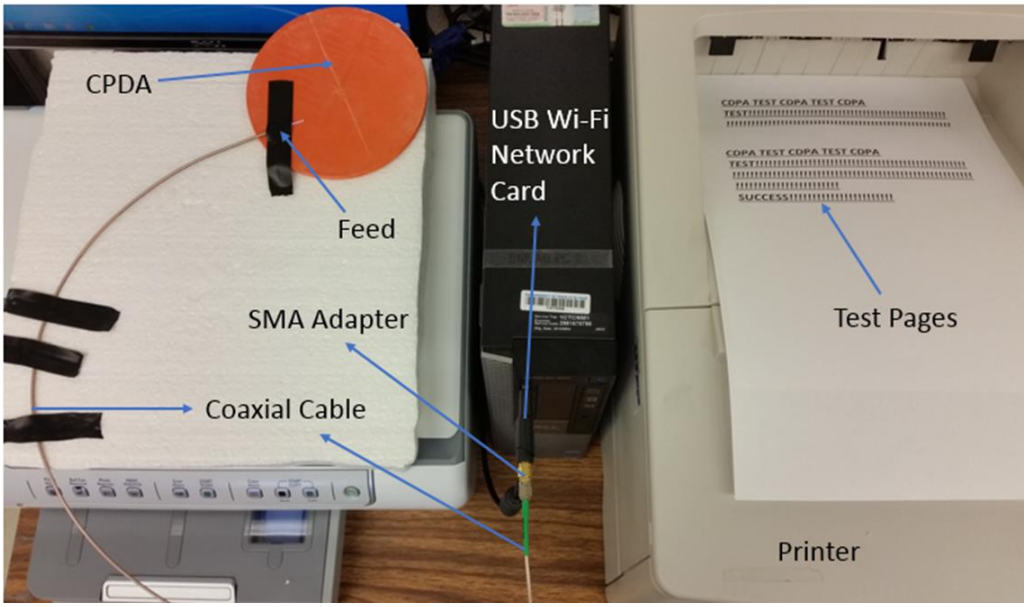

Figure 3.26: Picture of a close setup of the WiFi test.

Chapter 4: Conclusion

A dielectric prism antenna which operates with a leaky whispering gallery mode was developed. The dielectric prism antenna was developed in stages increasing in complexity starting from a one dimensional slab waveguide analysis. The next step was visualizing the fields with FDFD. The design was finalized with the commercial package HFSS for a fully rigorous simulation. To manufacture the antenna, a shell was 3D printed using a Makerbot Replicator 2X and the inside filled with dielectric powder. The antenna was then tested with a VNA and pattern measurements were taken in the anechoic chamber at the UTEP EM Lab. The dielectric prism antenna achieved a thickness of 1.5 mm with a relative permittivity of 20.

4.1 Future Work

This work can be expanded in the future by exploring more feed mechanisms. A vee dipole feed was chosen for its simplicity in this proof of concept work but maybe evanescent feeding would be more ideal. Further improvements can be made to the circulating mode by using a graded structure which would also allow for a thinner antenna. Achieving a lower relative permittivity is another area of improvement and this would increase the accessibility of the DPA. A more comprehensive study of gain is needed and work can be done to explore tailoring the radiation pattern to different needs.

References

[1] J. M. Floch, B. El Jaafari and A. El Sayed Ahmed. New compact broadband GSM/UMTS/LTE antenna realised by 3D printing. Presented at 2015 9th European Conference on Antennas and Propagation (EuCAP). 2015, .

[2] J. A. Andriambeloson and P. G. Wiid. Hyperband conical antenna design using 3D printing technique. Presented at Radio and Antenna Days of the Indian Ocean (RADIO), 2015. 2015, . DOI: 10.1109/RADIO.2015.7323417.

[3] M. Ahmadloo and P. Mousavi. Application of novel integrated dielectric and conductive ink 3D printing technique for fabrication of conical spiral antennas. Presented at Antennas and Propagation Society International Symposium (APSURSI), 2013 IEEE. 2013, . DOI: 10.1109/APS.2013.6711049.

[4] M. Mirzaee, S. Noghanian, L. Wiest and I. Chang. Developing flexible 3D printed antenna using conductive ABS materials. Presented at Antennas and Propagation & USNC/URSI National Radio Science Meeting, 2015 IEEE International Symposium On. 2015, . DOI: 10.1109/APS.2015.7305043.

[5] (2016). *nScrypt Printed Antennas*. Available: http://nscrypt.com/solutions/printed-antennas.

[6] I. Khromova, R. Gonzalo, I. Ederra, J. Teniente, K. Esselle and P. de Hon. Novel all-dielectric mm-wave horn antennas based on EBG structures. Presented at Antennas and Propagation (EUCAP), Proceedings of the 5th European Conference On. 2011, .

[7] M. Leib, A. Vollmer and W. Menzel. An ultra-wideband dielectric rod antenna fed by a planar circular slot. *IEEE Transactions on Microwave Theory and Techniques 59(4),* pp. 1082-1089. 2011. . DOI: 10.1109/TMTT.2011.2114050.

[8] S. Kobayashi, R. Lampe, R. Mittra and S. Ray. Dielectric rod leaky-wave antennas for millimeter-wave applications. *IEEE Transactions on Antennas and Propagation 29(5),* pp. 822-824. 1981. . DOI: 10.1109/TAP.1981.1142669.

[9] S. Long, M. McAllister and Liang Shen. The resonant cylindrical dielectric cavity antenna. *IEEE Transactions on Antennas and Propagation 31(3),* pp. 406-412. 1983. . DOI: 10.1109/TAP.1983.1143080.

[10] A. Petosa and A. Ittipiboon. Dielectric resonator antennas: A historical review and the current state of the art. *IEEE Antennas and Propagation Magazine 52(5),* pp. 91-116. 2010. . DOI: 10.1109/MAP.2010.5687510.

[11] I. M. Luk and K. W. Leung, *Dielectric Resonator Antennas.* Research Studies Press, 2003.

[12] R. K. Mongia. Reduced size metallized dielectric resonator antennas. Presented at Antennas and Propagation Society International Symposium, 1997. IEEE., 1997 Digest. 1997, . DOI: 10.1109/APS.1997.625406.

[13] R. K. Mongia, A. Ittibipoon and M. Cuhaci. Low profile dielectric resonator antennas using a very high permittivity material. *Electronics Letters 30(17),* pp. 1362-1363. 1994. . DOI: 10.1049/el:19940924.

[14] M. F. Ain, S. I. S. Hassan, M. A. Othman, B. M. Nawang, S. Sreekantan, S. D. Hutagalung and Z. A. Ahmad, "2.5 GHz batio3 dielectric resonator antenna," *Progress in Electromagnetics Research,* vol. 76, pp. 201-210, 2007.

[15] (2015, September 9). *Maxwell's Equations*. Available: http://emlab.utep.edu/ee5390cem/Lecture%209%20--%20Perfectly%20Matched%20Layer.pdf.

[16] (2015, December 8). *Finite Difference Method*. Available: http://emlab.utep.edu/ee5390cem/Lecture%2010%20--%20Finite%20Difference%20Method.pdf.

[17] Kane Yee. Numerical solution of initial boundary value problems involving maxwell's equations in isotropic media. *IEEE Transactions on Antennas and Propagation 14(3),* pp. 302-307. 1966. . DOI: 10.1109/TAP.1966.1138693.

[18] (2015, October 2). *Maxwell's Equations on a Yee Grid*. Available: http://emlab.utep.edu/ee5390cem/Lecture%2011%20--%20Maxwell's%20Equations%20on%20a%20Yee%20Grid.pdf.

[19] (2015, October 15). *FDFD implementation*. Available: http://emlab.utep.edu/ee5390cem/Lecture%2014%20--%20FDFD%20Implementation.pdf.

[20] (2015, September 30). *Finite-Difference Analysis of Waveguides*. Available: http://emlab.utep.edu/ee5390cem/Lecture%2012%20--%20Finite-Difference%20Analysis%20of%20Waveguides.pdf.

[21] R. C. Rumpf, "Simple implementation of arbitrarily shaped total-field/scattered-field regions in finite-difference frequency-domain," *Progress in Electromagnetics Research B,* vol. 36, pp. 221-248, 2012.

[22] Z. S. Sacks, D. M. Kingsland, R. Lee and Jin-Fa Lee. A perfectly matched anisotropic absorber for use as an absorbing boundary condition. *IEEE Transactions on Antennas and Propagation 43(12),* pp. 1460-1463. 1995. . DOI: 10.1109/8.477075.

[23] (2015, December 7). *Perfectly Matched Layer*. Available: http://emlab.utep.edu/ee5390cem/Lecture%209%20--%20Perfectly%20Matched%20Layer.pdf.

[24] C. Rodriguez, J. Avila and R. C. Rumpf, "Ultra-Thin 3D Printed All-Dielectric Antenna," *Submitted to Progress in Electromagnetics Research,* 2016.

Vita

Jose Antonio Avila was born in El Paso, Texas to Maria and Jose Avila. He is the younger of two siblings. He graduated from Del Valle High School in 2008. In December 2012 he was awarded his B.S. in Electrical Engineering from the University of Colorado at Colorado Springs. In the summer of 2013 he joined the EM Lab headed by Dr. Rumpf and enrolled to graduate school at the University of Texas at El Paso starting that fall. Currently he is pursuing a Doctoral Degree in Electrical Engineering in the area of electromagnetics, specifically all dielectric frequency selective surfaces.

Contact Information: jaavila5@miners.utep.edu

This thesis was typed by Jose Avila.